J. Fluid Mech. (2025), *vol.* 1008, A8, doi:10.1017/jfm.2025.106

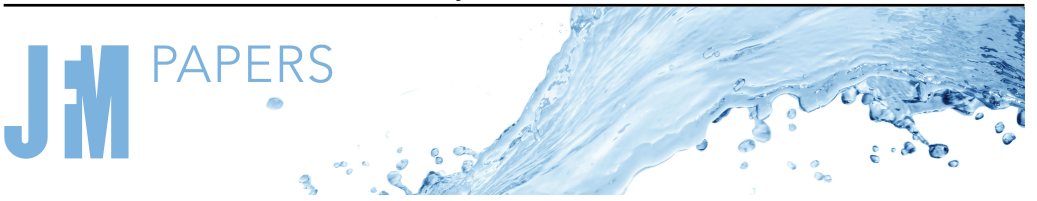

Ocean wave shield and cloak by a floating elastic annulus

Takahito Iida

Department of Naval Architecture and Ocean Engineering, Osaka University, Osaka 5650871, Japan
Corresponding author: Takahito Iida, iida@naoe.eng.osaka-u.ac.jp

(Received 26 August 2024; revised 18 January 2025; accepted 18 January 2025)

As new concepts to protect marine structures from ocean waves, we propose the use of a floating elastic annulus. In this paper, two types of annuli are demonstrated. The first is a 'wave shield', which creates a calm free surface within an inner domain of the annulus by preventing wave penetration. The second is a 'cloak', which not only creates a calm space within the inner domain but also prevents wave scattering outside the annulus. To evaluate the calmness of the inner domain of the annulus, an inlet wave energy factor is newly defined. The wave shield is designed to minimise the inlet wave energy factor to nearly zero. However, the cloak is designed to minimise both the inlet wave energy factor and scattered-wave energy which evaluates the amount of wave scattering at far-field. Each annulus consists of several horizontal concentric annular plates, and the flexural rigidities of the plates are optimised to minimise objective functions at a target frequency. Numerical simulations demonstrate that both the wave shield and the cloak can create calm free surfaces within their inner domains. In addition, the cloak effectively suppresses the outgoing scattering waves and reduces the resultant wave drift force.

Key words: surface gravity waves, wave scattering, elastic waves

1. Introduction

Ocean waves, typically spanning tens to hundreds of metres in wavelengths, are powerful and pose a significant threat to marine structures. Therefore, marine structures should be designed to survive these waves (Goda 2010). If a calm free surface can be created on an open sea, ocean space utilisation will be more convenient and expanded.

To reduce the wave action to structures, coastlines and harbours, floating breakwaters have been developed (see a review by Dai *et al.* 2018). Most of the concepts are for inshore, but some are developed for open sea utilisation (e.g. Xiao *et al.* 2016;

Cominelli *et al.* 2023). Breakwaters manipulate waves by controlling various physical mechanics, such as phase interaction, reflection (or scattering), refraction, breaking and friction (Sawaragi 1995). Among them, we focus on the wave energy conservation process (i.e. breaking and friction are not scoped).

Over the past decade, transformation-based wave manipulation (Leonhardt 2006; Pendry *et al.* 2006) has been studied in the water wave communities. In particular, the realisation of water wave cloaking has attracted much attention. Since the governing equation of shallow water waves is invariant under the coordinate transformation (Cummer & Schurig 2007), the methodologies of shallow water cloaking are well established (Farhat *et al.* 2008; Zareei & Alam 2015; Dupont *et al.* 2016; Iida & Kashiwagi 2018; Zhang *et al.* 2024). However, the transformation-based wave manipulation is not applicable to ocean waves because the governing equation of non-shallow water waves is not form-invariant (Porter 2017). Alternately, the cloaking by bending wave rays from the surface into the internal surface using the nonlinear resonance of the bottom topography was proposed for the intermediate-depth and stratified sea waves (Alam 2012). In the ocean engineering communities, however, the scattering cancellation-based cloaking has been studied (Porter & Newman 2014; Newman 2014; Iida *et al.* 2014, 2016, 2023). Sub-structures (such as columns or elastic plate) are arranged to surround an inner structure, and these are designed to cloak the inner structure from waves. The scattering cancellation-based cloaking realises almost zero outgoing scattering waves, and the existence of the inner structure cannot be detected even when waves are observed outside the cloak. As a result, the steady wave drift force does not act on the cloaked structure. Nevertheless, this cloaking does not create a calm free surface within the cloaked domain, and the cloaked structure still meets waves. Therefore, the wave exciting force is acting on the structure (Newman 2014). In addition, the optimal design of the cloak changes when the shape of the inner structure changes.

In light of previous studies, the term ‘cloaking’ encompasses two different states. The first is preventing the detection of an object by suppressing wave scattering outside the cloak. The second is protecting the object from wave influence by shielding it from wave penetration within the cloak. How much the object scatters waves can be estimated by the scattered-wave energy (Newman 2014; Iida *et al.* 2014), and the first state is achieved by reducing the scattered-wave energy. Scattering cancellation-based cloaking satisfies this first state. However, the second state is more critical for protecting marine structures from ocean waves.

Here, we study the second state, protection from invading waves, to create a calm free surface within an inner domain of a floating elastic annulus. We newly derive a mean energy density of waves entering into the inner domain of the annulus (namely inlet wave energy density). The calmness of the free surface within the inner domain is estimated by a metric called the inlet wave energy factor, which is defined by the ratio of the inlet wave energy density to the mean density of the plane waves. The second state is achieved by reducing the inlet wave energy factor.

The concept of the floating elastic annulus is described in figure 1. The annulus consists of L horizontal plates of which adjacent plates are rigidly connected. The elastic annulus is modelled as Kirchhoff's thin plate (Meylan & Squire 1994; Peter *et al.* 2004). The response of multi-connected elastic plates is solved by the developed eigenvalue matching method (Iida *et al.* 2023) based on Peter *et al.* (2004), where assumed thin-plate modelling was validated through the experiment (Meylan *et al.* 2015). It should be mentioned that the use of a floating elastic annulus to reduce waves has already been attempted (Loukogeorgaki & Kashiwagi 2019; Malenica *et al.* 2023). Nevertheless, performances were not dramatic because they assumed constant flexural rigidity throughout the annulus.

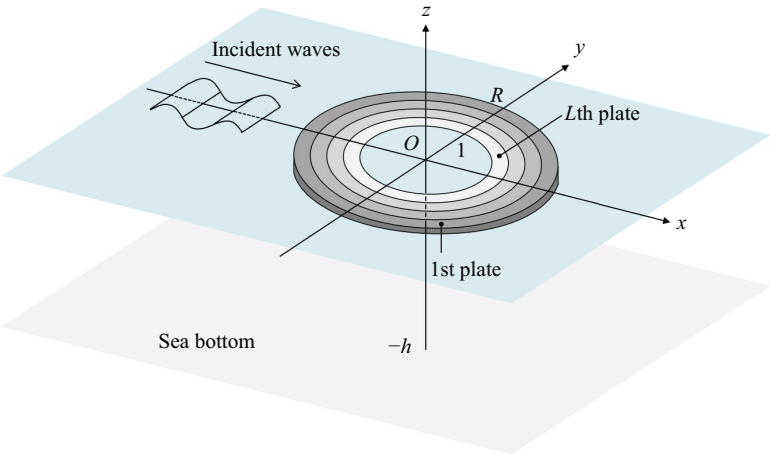

Figure 1. Schematic representation of floating annulus consisting of L horizontal concentric annular plates. The annulus is designed to serve as a wave shied and a cloak.

We design two types of annuli. The first annulus is designed as a 'wave shield' that creates a calm free surface within the inner domain of the annulus. This annulus is given by reducing the inlet wave energy factor (i.e. achieving the second state). The second annulus, however, is designed as a 'cloak' that blocks wave penetration and suppresses outgoing waves by achieving both first and second states. Flexural rigidities of the plates are optimised to maximise their performances at a target frequency. These parameters are designed within constraints based on a hypothetical scenario to demonstrate the feasibility of the concept, rather than as part of a practical application. We investigate the sensitivity of flexural rigidities to the inlet wave energy factor and scattered-wave energy and show that minimising them is typically in trade-off; achieving both states is challenging. Nevertheless, we demonstrate that this optimisation is successfully achieved by using the floating annulus with multi-plates. We numerically show that both the wave shield and the cloak can create a calm free surface within the inner domain of the annuli. In addition, the outgoing scattering waves can be also suppressed while maintaining a calm free surface using the cloak. The cloak also demonstrates that the wave drift force does not act on the cloak.

2. Theoretical descriptions

2.1. *Formulation of the boundary-value problem and its solutions*

We design both a floating wave shield and a floating cloak to illustrate the concepts for protecting marine structures from ocean waves. In that sense, a float must be applicable to deep water and performed for multi-directional sea waves. To meet these demands, we use a floating annulus, and the calm free surface is created within the inner radius of the annulus (inner domain). The concept and the problem definitions are shown in figure 1. A three-dimensional Cartesian coordinate system O-xyz is defined where the origin O is on the undisturbed (mean) free surface. The vertical axis z is positive in the upward direction. Although our target is deep sea, we formulate the problem so that numerical calculation can be performed at any water depth, with the flat bottom topography at $z = -h$. We consider an elastic annulus floating on the free surface of the sea of which the centre coincides with the origin. The outer and inner radii of the annulus are R and 1, respectively. The annulus consists of L horizontal concentric annular plates, and adjacent plates are rigidly connected. The annular plates are numbered from the outer to

the inner ($\ell = 1, 2, \ldots, L$), and the outer radius of each annular plate is denoted by $R^{(\ell)}$ (i.e. $R^{(1)} = R$ and $R^{(L+1)} = 1$). We do not use any active control force to create a calm space; the space will be made by the passive wave response of the annulus. We assume an elastic motion of the annulus can be described by Kirchhoff's thin plate theory (Meylan & Squire 1994; Peter *et al.* 2004). In addition, plane waves with single circular frequency incident on the annulus are considered. Since the annulus is axisymmetric, the wave response does not depend on the incident wave angle (i.e. omnidirectional). Therefore, we simply assume waves are propagating from the negative x direction.

The problem is formulated under the linear potential flow theory; we assume incompressible and inviscid fluid with the irrotational motion of the flow, and wave amplitude is sufficiently smaller than the wavelength. In addition, a time-harmonic solution of the response is considered. Therefore, we omit the time variable; a frequency domain analysis is carried out. All values are normalised (non-dimensionalised) by the incident wave amplitude, the fluid density, the gravitational acceleration and the inner radius of the annulus. The normalised governing equation and boundary conditions in the frequency domain are given as

$$\nabla^2\phi = 0 \quad -h \leqslant z \leqslant 0, \tag{2.1}$$

$$\frac{\partial\phi}{\partial z} - \omega^2\phi = 0 \quad z = 0,\ r < 1,\ R \leqslant r, \tag{2.2}$$

$$\left(\beta^{(\ell)}\nabla_\perp^4 - \omega^2\gamma + 1\right)\frac{\partial\phi}{\partial z} - \omega^2\phi = 0 \quad z = 0,\ R^{(\ell+1)} \leqslant r < R^{(\ell)}, \tag{2.3}$$

$$\frac{\partial\phi}{\partial z} = 0 \quad z = -h, \tag{2.4}$$

where ϕ is the complex amplitude of the velocity potential (i.e. $\Phi(\boldsymbol{x}, t) = \mathrm{Re}[\phi(\boldsymbol{x})\exp(-i\omega t)]$), ω is the circular frequency, and $\nabla = (\partial/\partial x, \partial/\partial y, \partial/\partial z)$ and $\nabla_\perp = (\partial/\partial x, \partial/\partial y)$ are the three-dimensional and horizontal gradient operators, respectively. In addition, $\beta^{(\ell)} = D^{(\ell)}/(\rho_w g a^4)$ and $\gamma = \rho_p t_p/(\rho_w a)$ are non-dimensional flexural rigidity and mass where ρ_w and ρ_p are the density of fluid and plate, g is the gravitational acceleration, a is the inner radius of the annulus, t_p is the thickness of the annulus, $D^{(\ell)} = E^{(\ell)}t_p^3/12(1-\nu^2)$ is the dimensional flexural rigidity, $E^{(\ell)}$ is the Young's modulus, and ν is Poisson's ratio. Here, (2.1) is the Laplace equation, (2.2) is the linearised free surface condition of water, (2.3) is the linearised surface condition on the ℓth plate and (2.4) is the sea bottom condition. Our previous study (Iida *et al.* 2023) revealed that changing flexural rigidity is more effective than that of mass for controlling waves. Therefore, we use different values of flexural rigidity for each plate (i.e. $\beta^{(\ell)}$), and the mass remains constant for all plates (i.e. γ). Except for this point, other formulations are the same as in Iida *et al.* (2023), and the detail can be seen in this reference (although notation is slightly changed).

To obtain the solution, the fluid domain is decomposed into an outer domain ($R \leqslant r$), plate's domains ($R^{(\ell+1)} \leqslant r < R^{(\ell)}$) and inner domain ($0 \leqslant r < 1$). Using the variable separation technique and spectral decomposition, the velocity potentials in these domains are given as

$$\begin{aligned}\phi_{outer} = {} & \frac{1}{\mathrm{i}\omega}\sum_{m=-\infty}^{\infty} \mathrm{i}^m\,\mathrm{J}_m(k_0 r)\,f_0(z)\,\mathrm{e}^{\mathrm{i}m\theta} \\ & + \frac{1}{\mathrm{i}\omega}\sum_{m=-\infty}^{\infty}\left\{a_{m0}\,\mathrm{H}_m^{(1)}(k_0 r)\,f_0(z) + \sum_{n=1}^{\infty} a_{mn}\,\mathrm{K}_m(k_n r)\,f_n(z)\right\}\mathrm{e}^{\mathrm{i}m\theta} \quad R \leqslant r,\end{aligned} \tag{2.5}$$

$$\phi_{plate}^{(\ell)} = \frac{1}{\mathrm{i}\omega}\sum_{m=-\infty}^{\infty}\left\{b_{m0}^{(\ell)}\,\mathrm{J}_m\left(\mu_0^{(k)}r\right)F_0^{(k)}(z) + \sum_{n=-2,n\neq 0}^{\infty} b_{mn}^{(\ell)}\,\mathrm{I}_m\left(\mu_n^{(\ell)}r\right)F_n^{(\ell)}(z) + c_{m0}^{(\ell)}\,\mathrm{H}_m^{(1)}\left(\mu_0^{(k)}r\right)F_0^{(k)}(z) + \sum_{n=-2,n\neq 0}^{\infty} c_{mn}^{(\ell)}\,\mathrm{K}_m\left(\mu_n^{(\ell)}r\right)F_n^{(\ell)}(z)\right\}\mathrm{e}^{\,\mathrm{i}m\theta}\; R^{(\ell+1)} \leqslant r < R^{(\ell)}, \tag{2.6}$$

$$\phi_{inner} = \frac{1}{\mathrm{i}\omega}\sum_{m=-\infty}^{\infty}\left\{d_{m0}\,\mathrm{J}_m(k_0 r)\,f_0(z) + \sum_{n=1}^{\infty} d_{mn}\,\mathrm{I}_m(k_n r)\,f_n(z)\right\}\mathrm{e}^{\,\mathrm{i}m\theta}\; 0 \leqslant r < 1, \tag{2.7}$$

where

$$f_n(z) = \begin{cases} \dfrac{\cosh k_0(z+h)}{\cosh k_0 h} & n=0, \\ \dfrac{\cos k_n(z+h)}{\cos k_n h} & n>0, \end{cases} \quad F_n^{(\ell)}(z) = \begin{cases} \dfrac{\cosh \mu_0^{(k)}(z+h)}{\cosh \mu_0^{(k)} h} & n=0, \\ \dfrac{\cos \mu_n^{(\ell)}(z+h)}{\cos \mu_n^{(\ell)} h} & n=-1,-2,n>0. \end{cases} \tag{2.8}$$

Here, $\mathrm{J}_m(\cdot)$, $\mathrm{H}_m^{(1)}(\cdot)$, $\mathrm{I}_m(\cdot)$ and $\mathrm{K}_m(\cdot)$ are the Bessel function of the first kind, the Hankel function of the first kind, and the modified Bessel functions of the first and second kinds, respectively. Functions $f_n(z)$ and $F_n^{(\ell)}(z)$ are solutions of the velocity potentials for z. In addition, k_n and $\mu_n^{(\ell)}$ are the wavenumbers of water waves and elastic waves of the ℓth plate which satisfy the following dispersion relations (Peter *et al.* 2004):

$$\omega^2 = \begin{cases} k_0 \tanh k_0 h, & n=0, \\ -k_n \tan k_n h, & n>0, \end{cases} \tag{2.9}$$

and

$$\frac{\omega^2}{\beta^{(\ell)}\mu_n^{(\ell)4} - \gamma\omega^2 + 1} = \begin{cases} \mu_0^{(k)} \tanh \mu_0^{(k)} h, & n=0, \\ -\mu_n^{(\ell)} \tan \mu_n^{(\ell)} h, & n=-1,-2,n>0. \end{cases} \tag{2.10}$$

Note that the wavenumber k_n has an infinite number of positive and real solutions, and $\mu_n^{(\ell)}$ also has an infinite number of positive and real solutions and two complex solutions $\mu_{-1}^{(\ell)} = (\mu_{-2}^{(\ell)})^*$ where these real parts are positive (Fox & Squire 1994). To obtain the complex amplitudes a_{mn}, $b_{mn}^{(\ell)}$, $c_{mn}^{(\ell)}$ and d_{mn}, further boundary conditions between adjacent domains are considered (see Appendix A). In this paper, the eigenvalue matching method (Peter *et al.* 2004; Iida *et al.* 2023) is employed to solve them.

2.2. *Inlet wave energy factor within the inner domain of the annulus*

To measure the calmness of the free surface within the inner domain of the annulus, we derive a mean wave energy density in the inner domain (namely, inlet wave energy density). At first, the time average of the kinetic energy density is given as

$$\overline{E_{kinetic}} = \frac{1}{4\pi}\int_{-h}^{0}\int_{0}^{2\pi}\int_{0}^{1}\mathrm{Re}\left[\frac{\partial\phi}{\partial r}\frac{\partial\phi^*}{\partial r} + \frac{1}{r^2}\frac{\partial\phi}{\partial\theta}\frac{\partial\phi^*}{\partial\theta} + \frac{\partial\phi}{\partial z}\frac{\partial\phi^*}{\partial z}\right] r\,\mathrm{d}r\mathrm{d}\theta\mathrm{d}z. \tag{2.11}$$

Since the incident wave energy is not distributed to local waves (i.e. energy conservation principle at far-field), the local wave component of (2.7) is not necessary to consider the energy balance. Therefore, substituting the first term of (2.7) into (2.11), the kinetic energy density in the inner domain is calculated as

$$\begin{aligned}\overline{E_{kinetic}} = \frac{1}{16}\sum_{m=-\infty}^{\infty}|d_{m0}|^2\Bigg[&\left(1+\frac{2k_0h}{\sinh 2k_0h}\right)\left\{\mathrm{J}'^2_{m-1}(k_0)+\left(1-\frac{(m-1)^2}{k_0^2}\right)\mathrm{J}^2_{m-1}(k_0)\right\}\\&+\left(1+\frac{2k_0h}{\sinh 2k_0h}\right)\left\{\mathrm{J}'^2_{m+1}(k_0)+\left(1-\frac{(m+1)^2}{k_0^2}\right)\mathrm{J}^2_{m+1}(k_0)\right\}\\&+2\left(1-\frac{2k_0h}{\sinh 2k_0h}\right)\left\{\mathrm{J}'^2_{m}(k_0)+\left(1-\frac{m^2}{k_0^2}\right)\mathrm{J}^2_{m}(k_0)\right\}\Bigg].\end{aligned} \tag{2.12}$$

Similarly, the time average of the potential energy density is obtained as

$$\begin{aligned}\overline{E_{potential}} &= \frac{1}{\pi}\overline{\int_0^{\zeta}\int_0^{2\pi}\int_0^{1} zr\,\mathrm{d}r\,\mathrm{d}\theta\,\mathrm{d}z}\\&= \frac{1}{4}\sum_{m=-\infty}^{\infty}|d_{m0}|^2\left\{\mathrm{J}'^2_{m}(k_0)+\left(1-\frac{m^2}{k_0^2}\right)\mathrm{J}^2_{m}(k_0)\right\}.\end{aligned} \tag{2.13}$$

The inlet wave energy density is given by the sum of these kinetic and potential energy densities, as

$$\begin{aligned}\overline{E_{inlet}} &= \overline{E_{kinetic}}+\overline{E_{potential}}\\&= \sum_{m=-\infty}^{\infty}|d_{m0}|^2\Bigg[\frac{\omega^2+\left(k_0^2-\omega^4\right)h}{16\omega^2}\left\{\mathrm{J}'^2_{m-1}(k_0)+\left(1-\frac{(m-1)^2}{k_0^2}\right)\mathrm{J}^2_{m-1}(k_0)\right\}\\&\quad+\frac{\omega^2+\left(k_0^2-\omega^4\right)h}{16\omega^2}\left\{\mathrm{J}'^2_{m+1}(k_0)+\left(1-\frac{(m+1)^2}{k_0^2}\right)\mathrm{J}^2_{m+1}(k_0)\right\}\\&\quad+\frac{3\omega^2-\left(k_0^2-\omega^4\right)h}{8\omega^2}\left\{\mathrm{J}'^2_{m}(k_0)+\left(1-\frac{m^2}{k_0^2}\right)\mathrm{J}^2_{m}(k_0)\right\}\Bigg].\end{aligned} \tag{2.14}$$

When the floating annulus is absent, the velocity potential of plane waves is of course represented by the first term of (2.5). Then, the mean wave energy density for any free surface position should be calculated by replacing d_{m0} in (2.14) with i^m. The result is obtained as

$$\overline{E_{plane}} = \overline{E_{kinetic}}+\overline{E_{potential}} = \frac{1}{4}+\frac{1}{4} = \frac{1}{2}. \tag{2.15}$$

Note that the relation

$$\sum_{m=-\infty}^{\infty}\left\{\mathrm{J}'^2_{m}(k_0)+\left(1-\frac{m^2}{k_0^2}\right)\mathrm{J}^2_{m}(k_0)\right\} = 1 \tag{2.16}$$

is used. The mean energy density (2.15) is the same result as the well-known one (Newman 2018*a*) where the dimensional expression is $\rho_w g\zeta^2/2$.

The calmness of the inner domain is evaluated by the ratio of the inlet wave energy density to the mean density of the plane wave, namely the inlet wave energy factor, defined by

$$\mathcal{F}_{inlet} \equiv \frac{\overline{E_{inlet}}}{\overline{E_{plane}}}. \tag{2.17}$$

The calm free surface is realised by $\mathcal{F}_{inlet} \to 0$.

It should be emphasised that the calmness of the inner domain should be evaluated by the energy throughout the inner domain. If the energy at a single point, such as the origin, is considered, there is a possibility that such a point could become a node of standing waves, which does not ensure calmness throughout the inner domain. In practice, it is simpler to minimise the wave amplitude $\sum_{m=-\infty}^{\infty} |d_{m0}|^2$ instead of (2.16). However, by using (2.16), the ratio to the incident wave energy can be defined as (2.17), and this makes physical interpretation easier than minimisation of the wave amplitude.

2.3. *Scattered-wave energy and wave drift force*

The amount of waves scattered by the annulus is evaluated by the scattered-wave energy (Iida *et al.* 2014). The energy conservation principle at far-field is given as (Kashiwagi *et al.* 2005)

$$W = \frac{1}{C_0 k_0 \omega} \sum_{m=-\infty}^{\infty} \left\{ \mathrm{Re}\left[\mathrm{i}^m a_{m0}^* \right] + |a_{m0}|^2 \right\} = 0, \tag{2.18}$$

where

$$C_0 = \frac{k_0}{\omega^2 + \left(k_0^2 - \omega^4\right)h}. \tag{2.19}$$

Note that (2.18) can be used for verification of the numerical code (this will be demonstrated in § 2.4). The scattered-wave energy is defined by the second term of (2.18), i.e.

$$W_S = \frac{1}{C_0 k_0 \omega} \sum_{m=-\infty}^{\infty} |a_{m0}|^2. \tag{2.20}$$

Here, a_{m0} is the complex amplitude of the outgoing scattering waves, and thus (2.20) indicates the energy of scattering waves. A zero scattering wave is realised by $W_S \to 0$.

The wave drift force, the steady component of the second-order hydrodynamic forces, acting on the annulus is also given by the complex amplitude of scattering waves (Kashiwagi *et al.* 2005), as

$$\overline{F_x} = \frac{1}{2C_0 \omega} \sum_{m=-\infty}^{\infty} \mathrm{Im}\left[2a_{m0} a_{m+1,0}^* + \mathrm{i}^m a_{m+1,0}^* + (-\mathrm{i})^{m+1} a_{m0} \right]. \tag{2.21}$$

As (2.21) indicates, the wave drift force becomes very small when no wave is scattered by the annulus.

2.4. *Design of the annulus*

We design the annulus as a wave shield to prevent waves from invading its inner domain. Additionally, we design another annulus as a cloak to block wave penetration and

suppress outgoing waves. Therefore, the following single-objective optimisation problem is considered:

$$\text{minimise } f = w_1 \mathcal{F}_{inlet} + w_2 W_S, \tag{2.22}$$

where w_1 and w_2 are the weights. For the wave shield, we consider $w_1 = 1$ and $w_2 = 0$. For the cloak, however, $w_1 = w_2 = 1$ is used as a simple allocation. Note that the original dimensions of $\mathcal{F}_{inlet}$ and W_S are different (although these are normalised here). The mean energy density has the dimension $\mathrm{kg\ s^{-2}}$, the inlet wave energy factor is dimensionless and the scattered-wave energy has the dimension $\mathrm{kg\ m^2\ s^{-3}}$. We do not consider $f = W_s$ (i.e. $w_1 = 0$ and $w_2 = 1$) because this optimal solution is given by $\beta^{(\ell)} \to 0$; the annulus is negligibly soft.

We solve the single optimisation (2.22) at non-dimensional wavenumber $k_0 = 1.0$ subject to $\nu = 0.25$, $\gamma = 0.05$ and the constraint $0.001 \leqslant \beta^{(\ell)} \leqslant 220$. We also assume the outer radius of the annulus is $R = 5.0$ and the radial widths of all plates are the same. This condition reflects the following scenario: a calm free surface with a radius of 16 m is created against typical ocean waves with a wavelength of 100 m (i.e. the period is 8 s in deep water). Assuming 2 m for the thickness of the annulus, the dimensional values of the constraint of Young's modulus are $9 \times 10^{-4} \sim 200$ GPa, where these minimum and maximum constraints correspond to the properties of rubber and steel. In addition, $\gamma = 0.05$ is equivalent to the density ratio $\rho_p/\rho_w = 0.4$ ($\rho_w = 1025\ \mathrm{kg\ m^{-3}}$ is considered). Note that this scenario is set up to demonstrate that the annulus can be designed within a feasible range, but it is not necessarily useful for practical applications (for instance, the outer radius is considerably larger than that of the cloaked domain).

To seek an optimum design, the covariance matrix adaptation evolution strategy (CMA-ES; Hansen 2016) is employed. The CMA-ES uses the covariance matrix of a multivariate normal distribution for updating a searching area, and efficient optimisations can be achieved even for non-separable and ill-conditioned problems. Since all the tuning parameters have default recommendations (Hansen 2016), the CMA-ES could be applied to various problems without devoting effort to tuning these parameters. To find the optimal cloak design, multi-objective optimisation would be more suitable. However, since we only have the in-house code for the single-objective optimisation, we solve (2.22) in this study.

For the numerical simulations, finite truncating numbers $M = 20$ and $N = 15$ are used for velocity potentials (see Appendix A). Then, the simulations demonstrate good energy conservation (2.18) with an accuracy of less than $O(10^{-14})$. The water depth is assumed $h = \lambda$ (wavelength) to ensure the deep water assumption throughout all the frequencies.

3. Numerical results and discussion

3.1. *Sensitivity study*

Before conducting the optimisation, we first investigate the sensitivity of the combinations of $\beta^{(\ell)}$ to the objective functions. We consider the two-plates case ($L = 2$), and the contour maps of $\log_{10}(\mathcal{F}_{inlet})$ and $\log_{10}(W_S)$ against $\beta^{(1)}$ (outer plate) and $\beta^{(2)}$ (inner plate) are plotted in figure 2. Here, common logarithm is used to highlight the differences among small values. Looking at figure 2(*a*), there is a peak around $(\beta^{(1)}, \beta^{(2)}) = (10, 15)$. As $\beta^{(1)}$ and $\beta^{(2)}$ increase, $\mathcal{F}_{inlet}$ decreases. Influences of $\beta^{(1)}$ and $\beta^{(2)}$ are not symmetrical; increasing $\beta^{(2)}$ results in a faster decrease in $\mathcal{F}_{inlet}$. The result of W_S in figure 2(*b*) has similar contour lines around $(\beta^{(1)}, \beta^{(2)}) = (10, 15)$, but this area becomes a valley (smaller than others). In addition, this also has another valley line around $\beta^{(2)} = 0.18(\beta^{(1)} - 130)$. In contrast to $\mathcal{F}_{inlet}$, W_S increases as $\beta^{(1)}$ and $\beta^{(2)}$ increase. These indicate that bigger flexural rigidity leads to more incident waves being scattered (or reflected) at the outer

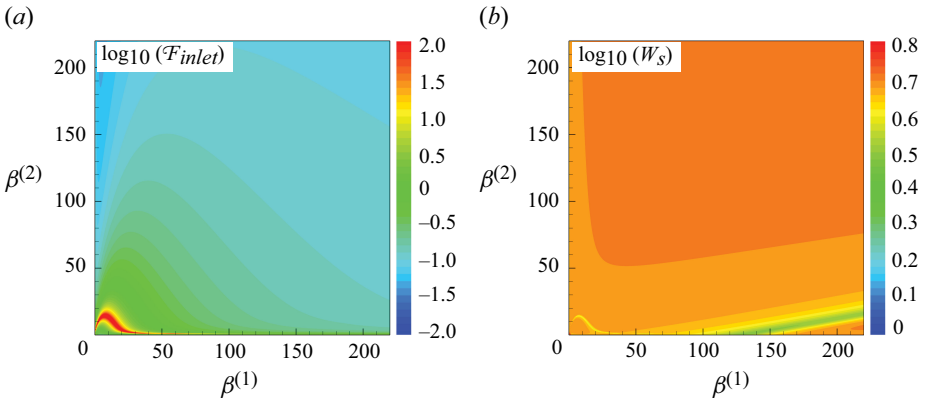

Figure 2. Sensitivity studies of the flexural rigidities $\beta^{(1)}$ (outer plate) and $\beta^{(2)}$ (inner plate) to (*a*) inlet wave energy factor $\mathcal{F}_{inlet}$ and (*b*) scattered-wave energy W_S. Results are presented using their common logarithm. Two plates case ($L = 2$) is considered where $\beta^{(1)}$ is of the outer plate and $\beta^{(2)}$is of the inner plate.

boundary of the annulus, and it results in the prevention of wave propagation into the inner domain. Therefore, $\mathcal{F}_{inlet} \to 0$ and $W_S \to 0$ are typically in trade-off. As the plate number L increases, the solution becomes more complex, and the objective function is likely to become a multi-modal function. Therefore, a metaheuristic optimisation approach (i.e. the CMA-ES) would be suitable to find an optimal solution.

3.2. *Optimisation*

The annuli are optimised to minimise $f = \mathcal{F}_{inlet}$ (inlet waves) and $f = \mathcal{F}_{inlet} + W_S$ (inlet waves and scattering waves), respectively. Optimisation results for the cases of the plate number $L = 1$, 2, 4, 8, and 16 are shown in table 1. Looking at the results for $f = \mathcal{F}_{inlet}$, the inlet wave energy factor is less than 10 % for all plate numbers and less than 1% when $L \geqslant 4$. However, the scattered-wave energy is maintained at $W_S \approx 5$, and thus incident waves are highly scattered by the annulus. As for the results for $f = \mathcal{F}_{inlet} + W_S$, cases of $L = 1$, 2 and 4 show a reduction only in the scattered-wave energy, while the inlet wave energy factor remains at 1. This indicates that the optimisation is performed to minimise W_S, and this results in $\beta^{(\ell)} \to 0$ ($\mathcal{F}_{inlet}$ is not exactly 1 because the mass γ is a finite value). However, the results of $L = 8$ and 16 demonstrate reductions of both inlet wave energy factor and scattered-wave energy. Especially, the result of $L = 16$ can dramatically suppress the scattered-wave energy while keeping a low inlet wave energy factor. In both objective functions, the inlet wave energy factor can be reduced to a sufficiently small level for practical purposes. Therefore, the structure of the wave shield is not unique.

Figure 3 shows a plot of $\beta^{(\ell)}$ along the radial direction of the annulus ($1 \leqslant r \leqslant 5$). The result of the wave shield is shown in figure 3(*a*), while the result of the cloak is in figure 3(*b*). Cases of $L = 8$ and 16 are shown. In figure 3(*a*), there is a peak around $2.5 \leqslant r \leqslant 4$, where $\beta^{(\ell)}$ reaches the maximum constraint value of 220. Outside this area, $\beta^{(\ell)}$ becomes small. In figure 3(*b*), there are two peaks for $L = 16$. At the peaks, $\beta^{(\ell)}$ reaches the maximum constraint; outside the peaks, it is nearly at the minimum constraint; and inside the peaks, it takes on intermediate values. Such a structure cannot be achieved by $L = 4$.

Snapshots of wave fields are plotted in figures 4 and 5, where plane waves are incident from the left-hand side of the figures. Figure 4 is the result for the wave shield and figure 5 is for the cloak. Panels (*a*,*c*) are the snapshots of wave patterns (imaginary parts of complex wave amplitude) and panels (*b*,*d*) are the wave amplitudes (magnitude of complex

Type	Objective function	Plate number L	Inlet wave energy factor $\mathcal{F}_{inlet}$	Scattered-wave energy W_S
Wave shield	$\mathcal{F}_{inlet}$	1	0.094	5.066
		2	0.047	4.987
		4	0.003	4.340
		8	0.002	5.356
		16	0.002	5.404
Cloak	$\mathcal{F}_{inlet} + W_S$	1	1.093	0.014
		2	1.049	0.018
		4	1.001	0.004
		8	0.076	0.029
		16	0.040	0.002

Table 1. Optimisation results of the annulus designed as the wave shield and the cloak.

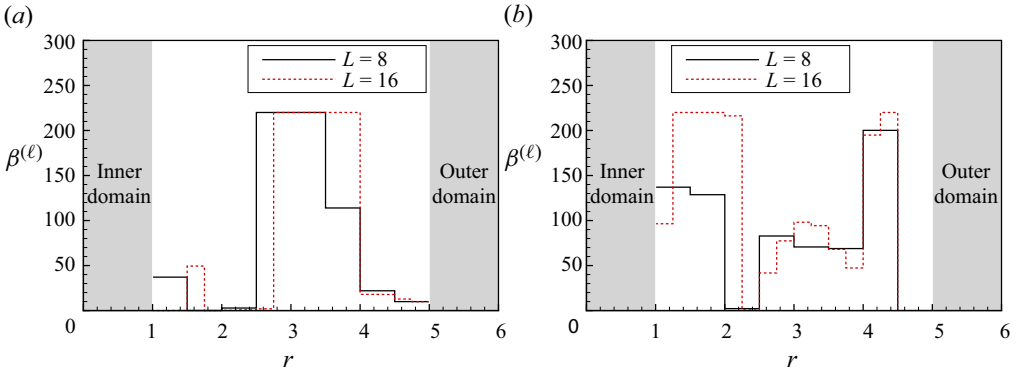

Figure 3. Spatial distributions of flexural rigidity $\beta^{(\ell)}$ along the radial direction of the annulus ($1 \leqslant r \leqslant 5$). (*a*) Optimised result for wave shields ($f = \mathcal{F}_{inlet}$). (*b*) Optimised result for cloaks ($f = \mathcal{F}_{inlet} + W_S$). Flexural rigidities are optimised within the constraint $0.001 \leqslant \beta^{(\ell)} \leqslant 220$.

wave amplitude). Case $L = 8$ is shown in panel (*a*,*b*), and $L = 16$ is in panel (*c*,*d*). Figure 4 shows that almost no waves propagate into the inner domain of the annulus, and elastic waves on the annulus are also small. These indicate that incident waves are scattered by the outer boundary of the annulus. As a result, there is a shadow behind the wave shield. In figure 5, wave penetration is also prevented by the cloak. In addition, there are a few outgoing scattering waves outside the cloak (see panel *b*,*d*). Especially, case $L = 16$ achieves seemingly perfect cloaking condition.

To investigate the frequency responses, inlet wave energy factor $\mathcal{F}_{inlet}$ and scattered-wave energy W_S against wavenumber k_0 are plotted in figures 6(*a*) and 6(*b*), respectively. The results are plotted on a semi-log graph. In figure 6(*a*), the line on $\mathcal{F}_{inlet} = 10^0 = 1$ indicates the same energy density as that of plane waves. In the long-wavelength region ($k_0 < 0.3$), the results converge to $\mathcal{F}_{inlet} = 1$ because the annulus merely follows the motion of the waves without scattering them. There are some periodic peaks due to resonance in the inner domain, which is typically known as moonpool resonance (e.g. Newman 2018*b*). Similar results are found from Malenica *et al.* (2023). Since the simulation is based on the linear potential theory, the amplified wave energy is unrealistically high. In real situations, these waves are dissipated by nonlinear processes, such as viscosity and wave-breaking. Except for these regions, all the annuli can reduce the inlet wave energy factor not only at optimised wavenumber $k_0 = 1.0$, but also at

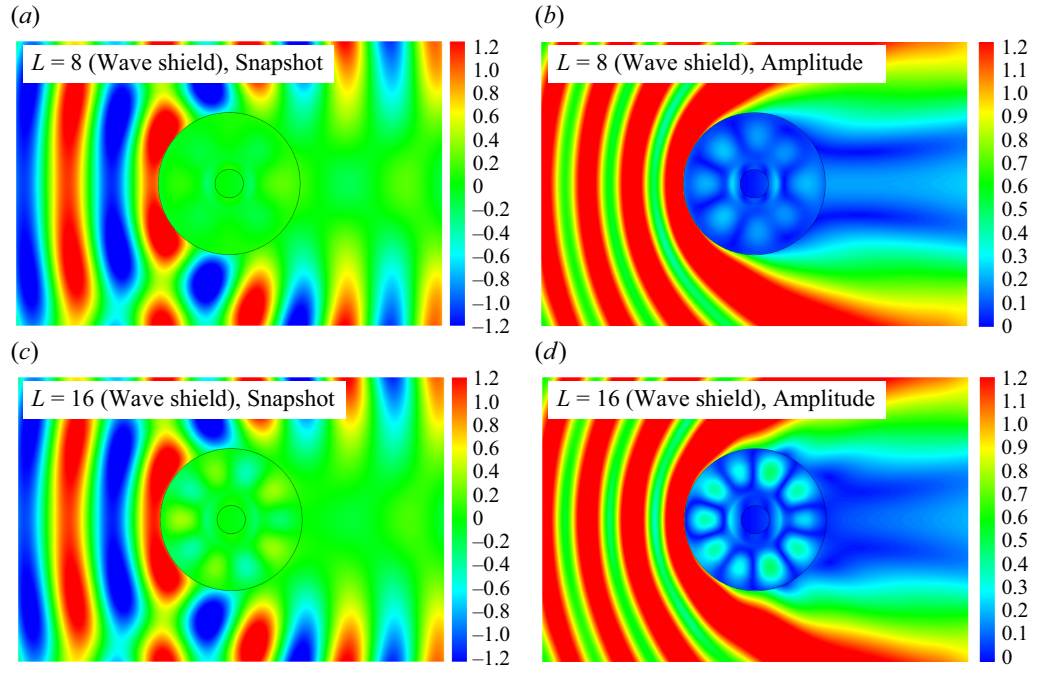

Figure 4. Wave fields for the 'wave shield' at wavenumber $k_0 = 1.0$. (*a*,*c*) Snapshots of wave patterns. (*b*,*d*) Wave amplitude. The results of plate numbers $L = 8$ and 16 are shown. Plane waves are incident from the left-hand side of the figures. The corresponding movie of panel (*c*) is available as supplementary movie 1 available at https://doi.org/10.1017/jfm.2025.106.

other frequencies. The optimisations for the wave shield achieve a greater reduction in the inlet wave energy factor compared with those for the cloak. In figure 6(*b*), the results of the cloak show dramatic reductions of the scattered-wave energy at $k_0 = 1.0$. Apart from this wavenumber, the scattered-wave energy remains of a similar order in all cases. Although the scattered-wave energy for $L = 16$ is lower than that for $L = 8$ at $k_0 = 1.0$, the order of the magnitude relationships is not consistent at other frequencies.

Finally, the wave drift force $\overline{F_x}$ acting on the annulus is shown in figure 7. The frequency responses of the wave drift force show similar behaviour to those of the scattered-wave energy as both are given by the scattering wave amplitude. As seen in figure 4(*d*), the wave shield scatters incident waves in front of the annulus at $k_0 = 1.0$. As a result, the large wave drift force acts on the annulus in the positive direction along the x-axis due to the action and reaction law. However, the cloak does not scatter waves outside the annulus (see figure 5*d*). Therefore, the wave drift force becomes almost zero at the target frequency as shown in figure 7.

3.3. *Further discussions*

In this section, we further discuss the proposed annuli, including their performances, limitations and potentials for further development. Using the wave shield, the inlet wave energy can be reduced over a wide range of frequencies compared with that in an open sea. However, periodic wave amplifications were observed due to resonance. This may endanger marine structures in the annulus. Using dissipative plates (e.g. Xiao *et al.* 2016; Liu *et al.* 2017) could be one of the solutions to reduce such a wave amplification.

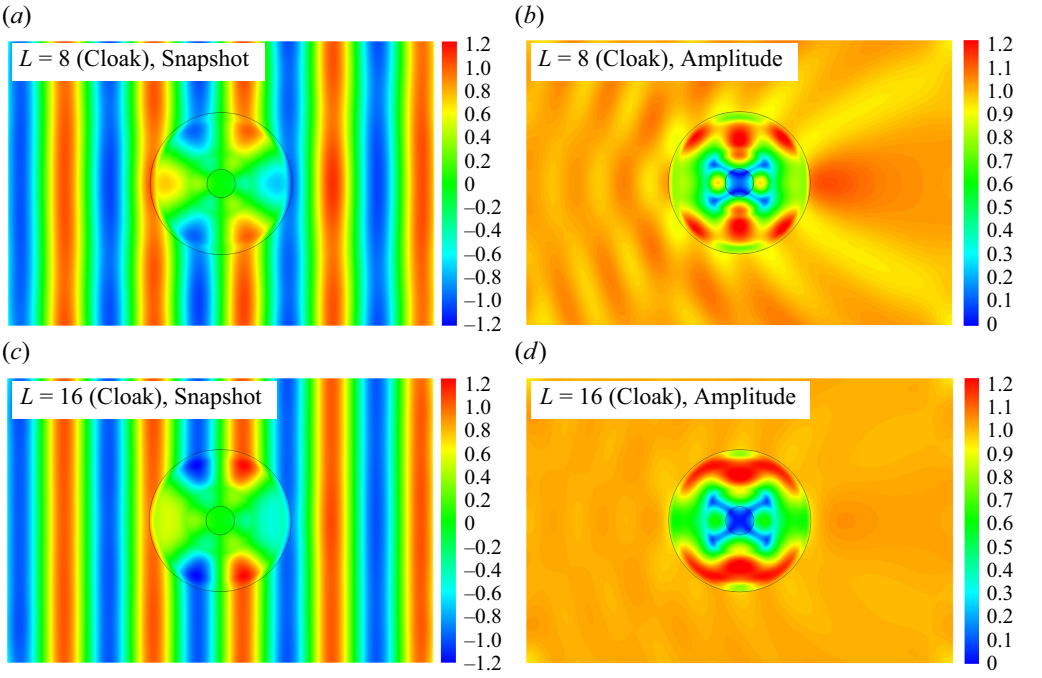

Figure 5. Wave fields for the 'cloak' at wavenumber $k_0 = 1.0$. (*a*,*c*) Snapshots of wave patterns. (*b*,*d*) Wave amplitude. The results of plate numbers $L = 8$ and 16 are shown. Plane waves are incident from the left-hand side of the figures. The corresponding movie of panel (*c*) is available as supplementary movie 2.

When the annulus is designed to minimise the inlet wave energy factor, a high wave drift force acts on the annulus due to wave scattering. Therefore, a strong mooring system is necessary to maintain a position. Another annulus, designed to minimise both inlet wave energy factor and scattered-wave energy, achieved the cloaking and resultant low wave drift force at the optimised frequency.

Optimisations were carried out at the single frequency $k_0 = 1.0$. For real applications, it is also demanded to perform over a range of frequencies. This could be achieved using a new objective function $\int_{\Delta k} f(k)\mathrm{d}k$ (e.g. Bobinski *et al.* 2018). However, achieving the desired frequency band performance would require a larger outer radius and an increased number of plates. This may reduce practical applicability and increase optimisation time. Therefore, it is not addressed in this paper.

We assumed a constant outer radius ($R = 5.0$) and mass ($\gamma = 0.05$). When the outer radius is small, the performance is insufficient. However, increasing the outer radius does not necessarily improve the performance. At present, $R = 5.0$ is the minimum size to achieve cloaking; however, for practical use, this annulus is too large compared with the inner cloaked domain. It is necessary to explore more practical sizes, such as by incorporating active control (e.g. Euvé *et al.* 2024). Heavy mass could give better performance. However, the density ratio to water is a limitation in design.

We developed the cloak based on the inlet-and-scattering-wave cancellation as the transformation-based cloak cannot be achieved for ocean waves. The coordinate transformation method is independent of wave frequency (Pendry *et al.* 2006). In many cases, anisotropic medium properties are realised using homogenisation methods (e.g. Zareei & Alam 2015; Dupont *et al.* 2016), and the homogenised performance can be maintained over a frequency band as long as the microstructure is sufficiently smaller

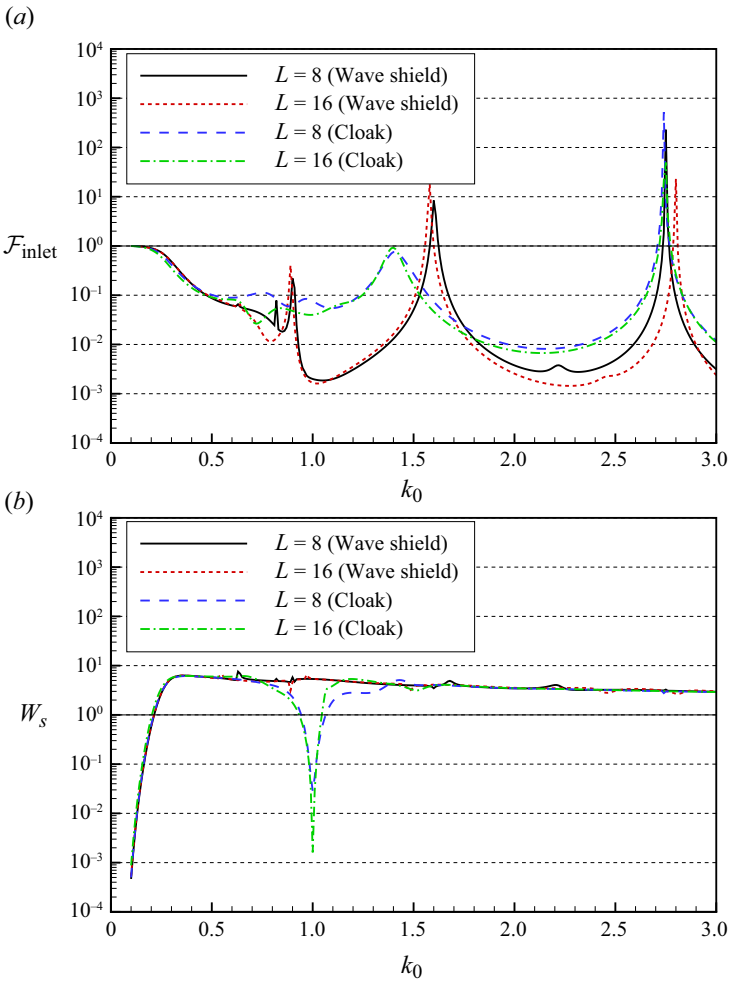

Figure 6. (*a*) Inlet wave energy factor $\mathcal{F}_{inlet}$ against wavenumber k_0. (*b*) Scattered-wave energy W_S against wavenumber k_0. Both panels are plotted on a semi-log graph. The annuli are optimised at $k_0 = 1.0$.

than the wavelength (Iida & Umazume 2020). Therefore, the transformation-based cloak is broadband. In addition, the physical interpretation is clear because this cloak is achieved by bending wave rays so that they bypass the inner cloaked domain. The present cloak, however, is currently limited to a single frequency as mentioned above. Moreover, the underlying mechanism of this cloak is not explicit because it involves a combination of various wave phenomena, such as reflection, refraction, trapping and superposition. Looking at supplementary movie 2, different behaviours are observed inside and outside $R = 2.5$: outside region ($2.5 \leqslant R \leqslant 5.0$), waves propagate as if they bypass the inner domain, which is similar to the transformation-based cloak; inside region ($1.0 \leqslant R \leqslant 2.5$), there are nodes and anti-nodes as if standing waves, which is a similar result to the wave shield (see supplementary movie 1). We do not expect this structure to be the unique solution to achieve the cloak; however, it may be insightful to theoretically describe the ocean wave cloak in the future. In any case, similar to the cloaking factor (Porter & Newman 2014), we expect the inlet wave energy factor to even contribute to studies of transformation-based cloaks and breakwaters as an important metric.

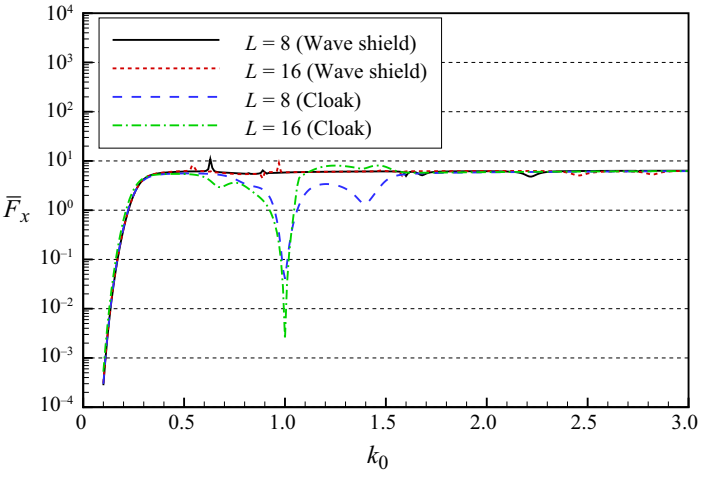

Figure 7. Wave drift force $\overline{F_x}$ acting on the annulus against wavenumber k_0 (semi-log graph).

We only demonstrated the potential of the wave shield and the cloak through numerical simulations based on the thin-plate assumption. Since this model assumes that the annulus only moves vertically in contact with the water surface, the annulus does not move in any other direction. However, in reality, motions in other modes (such as surge and sway) would be also induced. Therefore, a fully three-dimensional simulation is necessary for a detailed analysis. In addition, model experiments are also demanded to verify its feasibility. Although we assumed a closed annulus to simplify the problem, an opening is necessary for access to the inner domain. The influence of such an opening should also be investigated.

4. Conclusion

We presented the floating annuli that are used as a wave shield and a cloak. The annulus consists of L horizontal concentric annular plates, and each plate is elastic and thin. Based on the linear potential flow theory, the inlet wave energy factor is defined to estimate the calmness of the free surface within the inner domain of the annulus. From the sensitivity studies of flexural rigidities to the inlet wave energy factor and scattered-wave energy in the case of two plates, we found that minimising them is in trade-off. The flexural rigidity of each plate was designed to achieve the wave shield and the cloak, respectively. The numerical simulations demonstrated that the calm free surfaces are created within the inner domains of the optimised annuli. In addition, the cloak successfully suppressed the outgoing scattering waves, and the cloaking condition was accomplished. It was also shown that the wave drift force acting on the cloak can be almost zero. Since the annuli are axisymmetric, the performances are omnidirectional. These annuli could protect marine structures from ocean waves. We believe this would expand the possibility of ocean space utilisation.

Supplementary movies. Supplementary movies are available at https://doi.org/10.1017/jfm.2025.106.

Funding. This work was supported by JSPS KAKENHI Grant Number JP23K13504.

Declaration of interests. The author reports no conflict of interest.

Data availability statement. Data will be made available on request.

Appendix A. Boundary conditions

The coefficients a_{mn}, $b_{mn}^{(\ell)}$, $c_{mn}^{(\ell)}$ and d_{mn} in (2.5), (2.6) and (2.7) are unknown. By truncating the infinite series of azimuthal and radial modes to orders M and N, the number of unknown coefficients becomes $2(N+1)+2L(N+3)$. To solve these unknown coefficients, the same number of boundary conditions are required. Here, we consider the following boundary conditions.

(i) Matching conditions of the velocity potential between the outer free surface and the plate ($N+1$ equations).
(ii) Matching conditions of the radial derivative of the velocity potential between the outer free surface and the plate ($N+1$ equations).
(iii) Matching conditions of the velocity potential between adjacent plates ($(L-1)$ $(N+1)$ equations).
(iv) Matching conditions of the radial derivative of the velocity potential between adjacent plates ($(L-1)(N+1)$ equations).
(v) Matching conditions of the wave elevation between adjacent plates ($L-1$ equations).
(vi) Matching conditions of the radial derivative of the wave elevation between adjacent plates ($L-1$ equations).
(vii) Matching conditions of the bending moment between adjacent plates ($L-1$ equations).
(viii) Matching conditions of the shear force between adjacent plates ($L-1$ equations).
(ix) Free-free beam conditions; zero bending moment and shear force (four equations).
(x) Matching conditions of the velocity potential between the inner free surface and the plate ($N+1$ equations).
(xi) Matching conditions of the radial derivative of the velocity potential between the inner free surface and the plate ($N+1$ equations).

The boundary conditions (i) to (ix) are the same as those used by Iida *et al.* (2023), and details of equations are shown in the reference. Here, we only show the new boundary conditions (x) and (xi) as follows.

(i) Matching conditions of the velocity potential between the inner free surface and the plate ($N+1$ equations):

$$d_{m0}\,\mathrm{J}_m(k_0)A_{0q}+\sum_{n=1}^{N}d_{mn}\,\mathrm{I}_m(k_n)A_{nq}=b_{m0}^{(\ell)}\,\mathrm{J}_m\big(\mu_0^{(\ell)}\big)B_{0q}^{(\ell)}+\sum_{n=-2,n\neq0}^{N}b_{mn}^{(\ell)}\,\mathrm{I}_m\big(\mu_n^{(\ell)}\big)B_{nq}^{(\ell)}$$
$$+c_{m0}^{(\ell)}\,\mathrm{H}_m^{(\ell)}\big(\mu_0^{(\ell)}\big)B_{0q}^{(\ell)}+\sum_{n=-2,n\neq0}^{N}c_{mn}^{(\ell)}\,\mathrm{K}_m\big(\mu_n^{(\ell)}\big)B_{nq}^{(\ell)}. \tag{A1}$$

(ii) Matching conditions of the radial derivative of the velocity potential between the inner free surface and the plate ($N+1$ equations):

$$d_{m0}k_0\,\mathrm{J}'_m(k_0)A_{0q}+\sum_{n=1}^{N}d_{mn}k_n\,\mathrm{I}'_m(k_n)A_{nq}$$
$$=b_{m0}^{(\ell)}\mu_0^{(\ell)}\,\mathrm{J}'_m\big(\mu_0^{(\ell)}\big)B_{0q}^{(\ell)}+\sum_{n=-2,n\neq0}^{N}b_{mn}^{(\ell)}\mu_n^{(\ell)}\,\mathrm{I}'_m(\mu_n^{(\ell)})B_{nq}^{(\ell)}$$
$$+c_{m0}^{(\ell)}\mu_0^{(\ell)}\,\mathrm{H}_m^{(\ell)'}\big(\mu_0^{(\ell)}\big)B_{0q}^{(\ell)}+\sum_{n=-2,n\neq0}^{N}c_{mn}^{(\ell)}\mu_n^{(\ell)}\,\mathrm{K}'_m(\mu_n^{(\ell)})B_{nq}^{(\ell)}. \tag{A2}$$

Note that $q = 0, 1, \ldots, N$ and A_{nq} and $B_{nq}^{(\ell)}$ are given based on the eigenvalue matching method as

$$A_{nq} = \int_{-h}^{0} f_n(z) f_q(z) \mathrm{d}z, \quad B_{nq}^{(\ell)} = \int_{-h}^{0} F_n^{(\ell)}(z) f_q(z) \mathrm{d}z. \tag{A3}$$

References

Alam, M.-R. 2012 Broadband cloaking in stratified seas. *Phys. Rev. Lett.* **108** (8), 084502.

Bobinski, T., Maurel, A., Petitjeans, P. & Pagneux, V. 2018 Backscattering reduction for resonating obstacle in water-wave channel. *J. Fluid Mech.* **845**, R4.

Cominelli, S., Sinigaglia, C., Quadrelli, D.E. & Braghin, F. 2023 Optimal strategies to steer and control water waves. *Ocean Engng* **285**, 115346.

Cummer, S.A. & Schurig, D. 2007 One path to acoustic cloaking. *New J. Phys.* **9** (3), 45–45.

Dai, J., Wang, C.M., Utsunomiya, T. & Duan, W. 2018 Review of recent research and developments on floating breakwaters. *Ocean Engng* **158**, 132–151.

Dupont, G., Guenneau, S., Kimmoun, O., Molin, B. & Enoch, S. 2016 Cloaking a vertical cylinder via homogenization in the mild-slope equation. *J. Fluid Mech.* **796**, R1.

Euvé, L.-P., Pham, K., Petitjeans, P., Pagneux, V. & Maurel, A. 2024 Perfect active absorption of water waves in a channel by a dipole source. *J. Fluid Mech.* **990**, A9.

Farhat, M., Enoch, S., Guenneau, S. & Movchan, A. 2008 Broadband cylindrical acoustic cloak for linear surface waves in a fluid. *Phys. Rev. Lett.* **101** (13), 134501.

Fox, C. & Squire, V. A. 1994 On the oblique reflexion and transmission of ocean waves at shore fast sea ice. *Phil. Trans. R. Soc. Lond. A: Phys. Engng Sci.* **347** (1682), 185–218.

Goda, Y. 2010 *Random Seas and Design of Maritime Structures*. World scientific.

Hansen, N. 2016 The CMA evolution strategy: a tutorial. arXiv:1604.00772.

Iida, T. & Kashiwagi, M. 2018 Small water channel network for designing wave fields in shallow water. *J. Fluid Mech.* **849**, 90–110.

Iida, T., Kashiwagi, M. & He, G. 2014 Numerical confirmation of cloaking phenomenon on an array of floating bodies and reduction of wave drift force. *Intl J. Offshore Polar Engng* **24** (04), 241–246.

Iida, T., Kashiwagi, M. & Miki, M. 2016 Wave pattern in cloaking phenomenon around a body surrounded by multiple vertical circular cylinders. *Intl J. Offshore Polar Engng* **26** (01), 13–19.

Iida, T. & Umazume, K. 2020 Wave response of segmented floating plate and validation of its homogenized solution. *Appl. Ocean Res.* **97**, 102083.

Iida, T., Zareei, A. & Alam, M.-R. 2023 Water wave cloaking using a floating composite plate. *J. Fluid Mech.* **954**, A4.

Kashiwagi, M., Endo, K. & Yamaguchi, H. 2005 Wave drift forces and moments on two ships arranged side by side in waves. *Ocean Engng* **32** (5-6), 529–555.

Leonhardt, U. 2006 Optical conformal mapping. *Science* **312** (5781), 1777–1780.

Liu, H.-X., Chen, H.-L., Zhang, L., Zhang, W.-C. & Liu, M. 2017 Quadratic dissipation effect on the moonpool resonance. *China Ocean Engng* **31** (6), 665–673.

Loukogeorgaki, E. & Kashiwagi, M. 2019 Minimization of drift force on a floating cylinder by optimizing the flexural rigidity of a concentric annular plate. *Appl. Ocean Res.* **85**, 136–150.

Malenica, Š., Liang, H., Zheng, S. & Korobkin, A. 2023 Shielding effects of a floating ring-shaped poroelastic plate on a cylinder. In *Proceedings of 38th International Workshop on Water Waves and Floating Bodies*, pp. 1–4. International Workshop on Water Waves and Floating Bodies.

Meylan, M., Bennetts, L., Cavaliere, C., Alberello, A. & Toffoli, A. 2015 Experimental and theoretical models of wave-induced flexure of a sea ice floe. *Phys. Fluids* **27** (4), 041704.

Meylan, M. & Squire, V. A. 1994 The response of ice floes to ocean waves. *J. Geophys. Res.: Oceans* **99** (C1), 891–900.

Newman, J.N. 2014 Cloaking a circular cylinder in water waves. *Eur. J. Mech. B/ Fluids* **47**, 145–150.

Newman, J.N. 2018*a* *Marine Hydrodynamics*. The MIT press.

Newman, J.N. 2018*b* Resonant response of a moonpool with a recess. *Appl. Ocean Res.* **76**, 98–109.

Pendry, J.B., Schurig, D. & Smith, D.R. 2006 Controlling electromagnetic fields. *Science* **312** (5781), 1780–1782.

Peter, M.A., Meylan, M.H. & Chung, H. 2004 Wave scattering by a circular elastic plate in water of finite depth: a closed form solution. *Intl J. Offshore Polar Engng* **14** (2), 81–85.

Porter, R. 2017 *Cloaking in Water Waves*. World Scientific Handbook of Metamaterials and Plasmonics.

PORTER, R. & NEWMAN, J.N. 2014 Cloaking of a vertical cylinder in waves using variable bathymetry. *J. Fluid Mech.* **750**, 124–143.

SAWARAGI, T. 1995 *Coastal Engineering-Waves, Beaches, Wave-Structure Interactions*. Elsevier.

XIAO, L., KOU, Y., TAO, L. & YANG, L. 2016 Comparative study of hydrodynamic performances of breakwaters with double-layered perforated walls attached to ring-shaped very large floating structures. *Ocean Engng* **111**, 279–291.

ZAREEI, A. & ALAM, M.-R. 2015 Cloaking in shallow-water waves via nonlinear medium transformation. *J. Fluid Mech.* **778**, 273–287.

ZHANG, Z., IIDA, T., HE, G., MO, W., LIU, S., LUAN, Z. & JING, P. 2024 Boundary effects of anisotropic medium on cloaking under shallow-water waves. *Ocean Engng* **291**, 116485.